

Large-Eddy Simulation of the turbulent flow
within and above a forest canopy with the
LES-model ASAM

Zhou Putian

Master's Thesis

University of Helsinki

2013

Acknowledgements

First of all, I want to thank the Division of Atmospheric Sciences and Prof. Markku Kulmala for giving me financial support to do the research work related to my thesis. Furthermore, I would like to express my gratitude to my supervisor Dr. Michael Boy for his kindly help, many helpful suggestions and instructions for this thesis.

I want to thank my second supervisor Dr. Sampo Smolander for his patient guidance of the numerical model and the physical features of the PBL. I am also thankful for gaining much help on the characteristics of the forest canopy from Dr. Üllar Rannik. During my study trip at TROPOS, I really appreciated Dr. Oswald Knoth for providing me much help on the ASAM code. Besides, Michael Jähn and Ulrike Vogelsberg also gave me many helpful information on the ASAM code at TROPOS and by emails.

And thanks for everyone who helped me before.

Finally I would like to give my special thanks to my loving wife Qi Wenjuan. She is always standing beside me and supporting my work.



Contents

1	Introduction	7
1.1	The significance of researching atmospheric aerosol particles	7
1.2	Precursor gases in boreal forests	8
1.3	Modeling methods	9
1.4	The LES model	10
1.5	All Scale Atmospheric Model (ASAM)	11
1.6	Aims	11
1.7	Introduction to the following sections of this thesis	12
2	Theory	13
2.1	Introduction	13
2.2	Basic equation set of ASAM	13
2.3	The Favre averaging of basic equations	14
2.4	Parameterization methods for turbulent flow	16
2.4.1	$k - \epsilon$ method for the RANS model	17
2.4.2	Parameterization method for the LES model	18
2.5	Canopy parameterization methods	20
2.5.1	Canopy terms for momentum equations	20
2.5.2	Canopy terms for the RANS model	21
2.5.3	Canopy terms for the LES model	22
3	Methods	23
3.1	Introduction	23
3.2	Numerical method	23
4	Results and discussion	26
4.1	Introduction	26
4.2	Vertical profiles of spatially averaged fields	26
4.3	Cross sections of instantaneous fields	36
4.4	Results of the RANS model	41
5	Conclusions	45

ASAM (All Scale Atmospheric Model) is a numerical model developed and maintained by TROPOS (Leibniz Institute for Tropospheric Research). It implements moist compressible Navier-Stokes equations as its dynamic core. Depending on the parameterization methods, ASAM can be used as a LES (Large-eddy simulation) model or a RANS (Reynolds-averaged Navier-Stokes) model. In this study the forest canopy parameterization methods are added into ASAM for the two kinds of models. Some test cases for the turbulent flow inside and above the forest canopy in the PBL (Planetary Boundary Layer) are then performed by the modified ASAM.

The simulation results under neutral condition and weakly unstable condition are compared with previous research. It shows that the LES model is able to predict most essential features of the turbulent flow inside and above the canopy in the PBL, including the counter-gradient flux in the lower part of the canopy, the coupled relation between the downdraft regions and areas with sharp vertical shear of the wind velocity. While the RANS model can only simulate fields of averaged turbulence statistics, in particular case of horizontally homogeneous turbulence it can simulate several vertical profiles of horizontally averaged fields, e.g., the wind velocity and the Reynolds stress.

Keywords: LES, forest canopy, turbulence, planetary boundary layer

1

Introduction

1.1 The significance of researching atmospheric aerosol particles

In recent years atmospheric aerosols have been proved to have substantial impacts on global climate and air pollution [Arneth et al. (2009); Makkonen et al. (2012a)]. Human activities have also significantly influenced the coupling relations between aerosols, global climate and air quality [Kulmala et al. (2011)].

Since pre-industrial times anthropogenic activities have remarkably increased the emission of atmospheric aerosol particles [Pachauri and Reisinger (2007)]. The aerosol particles can influence the global climate in two ways, directly and indirectly [Haywood and Boucher (2000)]. The direct effect is a mechanism that changes radiative forcing by scattering and absorbing shortwave and long-wave radiation [Pachauri and Reisinger (2007); Ramanathan et al. (2001)]. Some aerosols (e.g., black carbon) exert a positive radiative forcing due to this mechanism, while others exert a negative one [Haywood and Boucher (2000)]. The overall direct effect on radiative forcing is estimated negative [Kulmala et al. (2011); Haywood and Schulz (2007)]. The indirect effect is a mechanism in which aerosol particles can act as cloud condensation nuclei (CCN) to influence the amount, albedo and lifetime of clouds. This process always has a cooling effect on the global climate [Lohmann and Feichter (2005)]. Although much research has been done to quantify the overall cooling effect

of atmospheric aerosols, the contribution of the aerosol particles to radiative forcing still remain largely uncertain due to the two complicated mechanisms mentioned above [Forster et al. (2007); Haywood and Boucher (2000)]. On the other hand, aerosol particles can also reduce visibility and air quality in urban areas, which deteriorates human health [Kulmala et al. (2011)]. Furthermore, air pollution is thought to be likely associated with the climate change [Arneth et al. (2009)].

So atmospheric aerosols both affect and respond to human life in many different ways, and the effects of aerosol on global climate still remain great uncertain [Makkonen et al. (2012b)]. Hence, we need to pay more attention to studying the chemical and physical processes of atmospheric aerosol particles.

1.2 Precursor gases in boreal forests

According to the formation mechanisms, aerosol particles can be divided into two broad categories, primary and secondary [Seinfeld and Pandis (2006)]. Primary aerosols are emitted directly into the atmosphere. They are formed from different sources, e.g., the burning of fossil fuels and vegetation, the combustion in industries and the emission of road transport [Kulmala et al. (2011)]. Secondary aerosols are created within the atmosphere by a series of chemical and physical processes (i.e., new particle formation and condensation growth) from precursor gases (i.e., sulphuric acid, ammonia, water vapor, organic vapors) [Kulmala (2003)]. The precursor gases can be produced by both natural processes and anthropogenic activities [Kulmala et al. (2001, 2011)].

In boreal forests, the emission and spatial distribution of precursor gases [Bäck et al. (2012)], the conversion of these gases to aerosol particles [Riipinen et al. (2011)], the transportation and turbulent mixing of them with the environment [?], and the influence of the turbulence on chemical and physical processes are all key issues in studying aerosol dynamics [Kulmala et al. (2001, 2011)]. Here we mean precursor gases mainly by volatile organic compounds (VOCs, e.g., isoprene, monoterpenes and sesquiterpenes) and semi-volatile organic compounds (SVOCs) [Ehn et al. (2012)]. In boreal forest regions the canopy plays a crucial role in

these issues in the planetary boundary layer (PBL). First, the forest canopy emits a high number of VOCs [Hakola et al. (2003); Tarvainen et al. (2005); Bäck et al. (2012)]. Some of the VOCs can react with other compounds in the air and are then oxidized to SVOCs [Kavouras et al. (1999); Riipinen et al. (2011)]. Moreover, some SVOCs are released directly from the vegetations [Ieda et al. (2006)]. These SVOCs are less volatile and may participate in atmospheric new particle formation [Riipinen et al. (2012)]. This process increases the concentration of aerosol particles inside and above the canopy and thus alters the spatial distribution of the aerosol particles in the whole PBL [Bonn et al. (2008)]. On the other hand, canopy drag can change the ground surface condition, wind profiles and also produce turbulence within and above the forest canopy, which significantly influences the advection and convection of aerosol particles in the PBL. Therefore, it is of great interest to study the emission, reactions and transportation of these chemicals in the PBL considering canopy effects.

1.3 Modeling methods

Measurements can provide many data sets but not in all the space-time points that we need, and applications of data statistics can provide relationships between different variables but not the cause and effect behind the phenomena. Thus, we need to use numerical models to compensate for these deficiencies and obtain a better understanding of the chemical and physical processes in the atmosphere.

Previous numerical models have shown many valuable results of the canopy effects in the PBL, but they did not combine chemistry directly with 3-dimensional (3D) turbulent transport and interactions to reveal more details of how the chemicals are emitted, react and transport in the PBL considering canopy effects. For example, SOSA (model to simulate the concentration of organic vapours and sulphuric acid) was used to research the emission, reactions and transportation of the chemicals in Hyytiälä [Boy et al. (2011)]. However, it is a 1-dimensional (1D) model and cannot simulate all details of turbulent transport and interactions. Some meteorological models only concerned the turbulent flow within and above the canopy, but they

did not implement explicit chemistry or aerosol parts inside them [Aumond et al. (2013)].

Therefore, we want to develop a model combining all of these parts to further the research on these phenomena. As this is complex work, in this thesis we will first focus on the meteorological part. As we know, two kinds of parameterization methods for simulating the turbulent flow are usually implemented in meteorological models. One is the method using Reynolds-Averaged Navier-Stokes (RANS) equations; the other is the Large-Eddy Simulation (LES). The RANS method calculates the average fluid motion and some turbulence statistics, demanding less computational cost, while the LES method has the advantage in showing transient turbulence in the flow, but requires greater computational cost. So the LES is more suitable for our research. But we will also use the RANS method for comparisons.

1.4 The LES model

The LES model is a kind of numerical model mainly used for simulating turbulence in fluid. It only directly simulates the large eddies while parameterizing eddies smaller than the filter size. Therefore, the computational cost of the LES model is less than that of the Direct Numerical Simulation (DNS) model. This makes it feasible to simulate the turbulent flow in a more extensive spatial and temporal scale as well as in more complex flow configurations. Hence, it is a powerful tool in studying the complicated physical processes in the PBL. In fact, many studies have applied LES models in their research of turbulence structure in the PBL [e.g., Moeng (1984); Saiki et al. (2000); Moeng et al. (2004)].

Furthermore, some published articles also used LES models for the canopy layer in the PBL [e.g., Shaw and Shumann (1992); Shen and Leclerc (1997)]. These previous studies demonstrated that the LES model is also a powerful mean of revealing the turbulence structure just above and within the canopy layer. In recent years, LES models have been more and more used in studying the turbulence patterns above and inside inhomogeneous canopies with higher and higher resolutions [Aumond et al. (2013); Gavrilov et al. (2011); Schlegel et al. (2012)].

1.5 All Scale Atmospheric Model (ASAM)

For our research we used ASAM [http://asamwiki.tropos.de/index.php/Main_Page] as the RANS and LES models. ASAM is a developing research code developed and maintained by TROPOS (Leibniz Institute for Tropospheric Research). It implements the moist compressible Euler equation set in its dynamic core. More details of governing equations can be found in Bryan and Fritsch (2002). Besides, it has several optional modules to manipulate different physical processes, for example, the radiation module and the microphysics module. It also contains several parameterization methods for turbulence. In our research we implemented the $k - \epsilon$ method for the RANS model, and for LES model we used an extension of Smagorinsky model which was already widely used in many LES models [Herzog et al. (2002)]. However, ASAM did not contain a canopy module. So in order to parameterize and simulate the turbulence above and within the canopy layer in the PBL, we added a canopy module into ASAM following previous studies. In this thesis, only the dynamic effects of a homogeneous canopy layer was considered.

Researchers at TROPOS have tested many benchmarks and other cases for ASAM, which ensures that it is reliable and appropriate for our research [Hinneburg and Knoth (2005); Horn (2012)]. The model was installed at the IT Center for Science (CSC) in Espoo, Finland in spring 2012. Thus parallel computation was available for our test cases.

1.6 Aims

In our project, we plan to develop a new model by combining the 3D meteorological model ASAM with a canopy module, an emission module, a chemistry module and an aerosol module. The canopy module has already been added in ASAM and its feasibility will be verified in this thesis. In future we will implement the emission module from MEGAN (Model of Emissions of Gases and Aerosols from Nature, [Guenther et al. (2012)]) as well as the chemistry and aerosol modules from SOSAA (SOSA and Aerosols) into ASAM. With the modified ASAM we aim to investigate

some interesting physical and chemical processes by the turbulent flow inside and above the boreal forest canopy. These processes may include, e.g., the emission of VOCs, the chemical reactions, the transportation, formation, growth and removal processes of aerosols.

Meanwhile, we will cooperate with Dr. Natalia Babkovskaia (a postdoc researcher in our Division) to combine this LES model with her DNS model, investigating the physical and chemical processes within clouds.

1.7 Introduction to the following sections of this thesis

In section 2, we will first give a brief introduction to ASAM. Then the parameterization methods used in RANS model and LES model are described in detail. The parameterization methods of canopy layer for these two models are also elucidated in this section. Section 3 presents the numerical method used for our simulations. The simulation results of 3-dimensional (3D) runs of ASAM will be shown in section 4. Discussions of the results are contained as well, for example, the consistence with other research, the comparisons between the simulation results and the observed data, the differences of the results between the RANS model and the LES model, etc. The conclusions are given in section 5.

2

Theory

2.1 Introduction

In this chapter we will first give an introduction to the dynamic core of ASAM, including the basic equation set, the Favre averaging of these equations, the parameterization methods for Reynolds stress tensor and subgrid scale eddies. Then the canopy parameterization methods for RANS and LES models are elucidated. This chapter mainly refers to the ASAM wiki page [http://asamwiki.tropos.de/index.php/Main_Page] and the master thesis of Elmar Filaus [Filaus (2007)].

2.2 Basic equation set of ASAM

ASAM is used for atmospheric simulations of all scales, it uses the moist compressible Euler equation set published by Bryan and Fritsch [Bryan and Fritsch (2002)] as its dynamic core. In this thesis we do not consider the moist processes, so the basic

equations for dry compressible air flow in vector form are as follows,

$$\frac{\partial \rho}{\partial t} + \nabla \cdot (\rho \mathbf{v}) = 0 \quad (2.1)$$

$$\frac{\partial(\rho \mathbf{v})}{\partial t} + \nabla \cdot (\rho \mathbf{v} \mathbf{v}) = -\nabla p + \rho \mathbf{g} - 2\boldsymbol{\Omega} \times (\rho \mathbf{v}) \quad (2.2)$$

$$\frac{\partial(\rho \theta)}{\partial t} + \nabla \cdot (\rho \mathbf{v} \theta) = Q_\theta \quad (2.3)$$

$$p = \rho R_d \theta \left(\frac{p}{p_0} \right)^{\kappa_d} \quad \text{or} \quad (2.4)$$

$$p = \left(\frac{\rho R_d \theta}{p_0^{\kappa_d}} \right)^{1/(1-\kappa_d)} \quad (2.5)$$

Where

$$\kappa_d = \frac{R_d}{c_{pd}} \quad (2.6)$$

$$R_d = \frac{R}{M} \quad (2.7)$$

R is the gas constant, R_d is the specific gas constant of dry air. M is the molar mass of dry air. Q_θ contains the sources and sinks of the heat energy. The meanings of other symbols are shown in Table 2.1. For simplicity we rewrite equations (2.1) to (2.3) in Cartesian coordinate using Einstein notation as follows,

$$\frac{\partial \rho}{\partial t} + \frac{\partial}{\partial x_j} (\rho u_j) = 0 \quad (2.8)$$

$$\frac{\partial(\rho u_i)}{\partial t} + \frac{\partial}{\partial x_j} (\rho u_i u_j) = -\frac{\partial p}{\partial x_i} - 2\rho \epsilon_{ijk} \Omega_j u_k + \rho g_i \quad (2.9)$$

$$\frac{\partial(\rho \theta)}{\partial t} + \frac{\partial}{\partial x_j} (\rho u_j \theta) = Q_\theta \quad (2.10)$$

Here $x_i = x, y, z$ for $i = 1, 2, 3$ and $u_i = u, v, w$ in horizontal and vertical directions. ϵ_{ijk} is the permutation symbol. Ω_j and g_i are the components of the angular velocity of earth and the gravitational acceleration, respectively.

2.3 The Favre averaging of basic equations

We have already had the basic equations, however, numerical models (except DNS models) do not solve the partial differential equation set directly. For example,

Table 2.1: Symbol table

Symbol	Name	Unit
ρ	air density	kg/m ³
t	time	s
$\mathbf{v}(u, v, w)$	velocity vector	m/s
p	air pressure	Pa
\mathbf{g}	gravitational acceleration	m/s ²
θ	potential temperature	K
p_0	reference pressure (10 ⁵ Pa)	Pa
c_{pd}	specific heat capacity at constant pressure for dir air	J/(kg·K)

RANS models only give the time-averaged solutions and LES models only resolve large scales of the fluid flow. So for these two kinds of models we need to first derive the corresponding equations using time-averaging and spatial filtering.

Here we will introduce the Reynolds averaging and Favre averaging at first. Reynolds averaging can decompose an independent variable ϕ into two parts, time-averaged part $\bar{\phi}$ and fluctuating part ϕ' . Similarly, Favre averaging also gives a mean part $\hat{\phi}$ and a perturbation ϕ'' , but here the average is density weighted. The formulas are shown as follows,

$$\phi = \bar{\phi} + \phi' \quad (2.11)$$

$$\phi = \hat{\phi} + \phi'' \quad (2.12)$$

$$\hat{\phi} = \frac{\overline{\rho\phi}}{\bar{\rho}} \quad (2.13)$$

We should notice that for Reynolds average, $\overline{\phi'} = 0$, while for Favre average $\overline{\phi''} \neq 0$, $\overline{\rho\phi''} = 0$. Making Reynolds average on equations (2.8) to (2.10) and substitute Favre

averaged variables into them, we can get,

$$\frac{\partial \bar{\rho}}{\partial t} + \frac{\partial}{\partial x_j}(\bar{\rho} \hat{u}_j) = 0 \quad (2.14)$$

$$\frac{\partial(\bar{\rho} \hat{u}_i)}{\partial t} + \frac{\partial}{\partial x_j}(\bar{\rho} \hat{u}_i \hat{u}_j) = -\frac{\partial \bar{p}}{\partial x_i} - 2\bar{\rho} \epsilon_{ijk} \Omega_j \hat{u}_k + \bar{\rho} g_i - \frac{\partial \tau_{ij}}{\partial x_j} \quad (2.15)$$

$$\frac{\partial(\bar{\rho} \hat{\theta})}{\partial t} + \frac{\partial}{\partial x_j}(\bar{\rho} \hat{u}_j \hat{\theta}) = \bar{Q}_\theta - \frac{\partial H_j}{\partial x_j} \quad (2.16)$$

Where

$$\tau_{ij} = \overline{\rho \hat{u}_i \hat{u}_j} - \bar{\rho} \hat{u}_i \hat{u}_j \quad (2.17)$$

$$H_j = \overline{\rho \hat{u}_j \hat{\theta}} - \bar{\rho} \hat{u}_j \hat{\theta} \quad (2.18)$$

For RANS models the average is for time, so

$$\begin{aligned} \tau_{ij} &= \overline{\rho \hat{u}_i \hat{u}_j} - \bar{\rho} \hat{u}_i \hat{u}_j \\ &= \overline{\rho u_i u_j} - \bar{\rho} \hat{u}_i \hat{u}_j \\ &= \overline{\rho(\hat{u}_i + u_i'')(\hat{u}_j + u_j'')} - \bar{\rho} \hat{u}_i \hat{u}_j \\ &= \hat{u}_i \overline{\rho u_j''} + \hat{u}_j \overline{\rho u_i''} + \overline{\rho u_i'' u_j''} \\ &= \overline{\rho u_i'' u_j''} \end{aligned} \quad (2.19)$$

Similarly,

$$H_j = \overline{\rho u_j'' \theta''} \quad (2.20)$$

However, τ_{ij} and H_j do not satisfy the formulas (2.19) and (2.20) for spatial average. So formulas (2.19) and (2.20) are used in the RANS model while (2.17) and (2.18) are used in the LES model.

2.4 Parameterization methods for turbulent flow

Now the 5 basic equations have 14 unknown variables $\bar{\rho}$, \hat{u}_i , $\hat{\theta}$, τ_{ij} and H_j , considering τ_{ij} is a symmetric tensor. So they are far from closed. An ordinary way to close the

basic equation set is to calculate τ_{ij} and H_j using the averaged variables $\bar{\rho}$, \hat{u}_i and $\hat{\theta}$. In ASAM they are computed in the following way,

$$\tau_{ij} = \bar{\rho}\nu_m \frac{\partial \hat{u}_i}{\partial x_j} \quad (2.21)$$

$$H_j = \bar{\rho}\nu_h \frac{\partial \hat{\theta}}{\partial x_j} \quad (2.22)$$

Here ν_m and ν_h are the eddy-viscosity coefficients for momentum and scalars, respectively. Their unit is $[\text{m}^2/\text{s}]$. In the RANS model and the LES model we use different parameterization methods to obtain ν_m and ν_h .

2.4.1 $k - \epsilon$ method for the RANS model

In ASAM $k - \epsilon$ method can be used to close the basic equations in the RANS model. The additional equations for calculating the eddy-viscosity coefficients are,

$$\frac{\partial}{\partial t}(\bar{\rho}\hat{k}) + \frac{\partial}{\partial x_j}(\bar{\rho}\hat{u}_j\hat{k}) = \frac{\partial}{\partial x_j} \left(\frac{\bar{\rho}\nu_m}{\sigma_k} \frac{\partial \hat{k}}{\partial x_j} \right) + P - \bar{\rho}\hat{\epsilon} \quad (2.23)$$

$$\frac{\partial}{\partial t}(\bar{\rho}\hat{\epsilon}) + \frac{\partial}{\partial x_j}(\bar{\rho}\hat{u}_j\hat{\epsilon}) = \frac{\partial}{\partial x_j} \left(\frac{\bar{\rho}\nu_m}{\sigma_\epsilon} \frac{\partial \hat{\epsilon}}{\partial x_j} \right) + C_{1\epsilon} \frac{\hat{\epsilon}}{\hat{k}} P - C_{2\epsilon} \bar{\rho} \frac{\hat{\epsilon}^2}{\hat{k}} \quad (2.24)$$

Here k is the Turbulent Kinetic Energy (TKE) with unit $[\text{m}^2/\text{s}^2]$ and ϵ is the dissipation rate of TKE with unit $[\text{m}^2/\text{s}^3]$. P is the production term of TKE, it is calculated under Kato-Launder modification [Kato and Launder (1993)] in the following way,

$$P = \bar{\rho}\nu_m S O \quad (2.25)$$

$$S = \sqrt{\frac{1}{2} \left(\frac{\partial \hat{u}_i}{\partial x_j} + \frac{\partial \hat{u}_j}{\partial x_i} \right)^2} \quad (2.26)$$

$$O = \sqrt{\frac{1}{2} \left(\frac{\partial \hat{u}_i}{\partial x_j} - \frac{\partial \hat{u}_j}{\partial x_i} \right)^2} \quad (2.27)$$

$C_{1\epsilon}$, $C_{2\epsilon}$ and C_μ are all constants,

$$C_{1\epsilon} = 1.44, \quad C_{2\epsilon} = 1.92, \quad C_\mu = 0.09 \quad (2.28)$$

σ_k and σ_ϵ are Prandtl numbers for k and ϵ , respectively. They are also constants,

$$\sigma_k = 1.0, \quad \sigma_\epsilon = \frac{\kappa^2}{C_\mu^{1/2}(C_{2\epsilon} - C_{1\epsilon})} \approx 1.111, \quad \kappa = 0.4 \quad (2.29)$$

Here κ is the von-Karman constant. Finally ν_m and ν_h can be calculated as,

$$\nu_m = C_\mu \frac{\hat{k}^2}{\hat{\epsilon}} \quad (2.30)$$

$$\nu_h = \nu_m \quad (2.31)$$

2.4.2 Parameterization method for the LES model

A modified Smagorinsky model [Herzog et al. (2002)] is used for the LES model in ASAM. In this method the eddy-viscosity coefficients are computed as follows.

First, we also need an additional equation for k just like in $k - \epsilon$ method,

$$\frac{\partial}{\partial t}(\bar{\rho}\hat{k}) + \frac{\partial}{\partial x_j}(\bar{\rho}\hat{u}_j\hat{k}) = \frac{\partial}{\partial x_j} \left(\bar{\rho}\nu_m \frac{\partial \hat{k}}{\partial x_j} \right) + P + B - C_\epsilon \frac{\bar{\rho}\hat{k}^{3/2}}{\lambda} \quad (2.32)$$

Where P is the same as that in the $k - \epsilon$ method and B is the buoyancy effect,

$$P = \bar{\rho}\nu_m S\Omega \quad (2.33)$$

$$B = -\bar{\rho}\nu_h N^2 \quad (2.34)$$

$$N^2 = \frac{g}{\hat{\theta}} \frac{\partial \hat{\theta}}{\partial z} \quad (2.35)$$

λ satisfies the relationship as follows,

$$\lambda = \begin{cases} \text{MIN} \left(\Lambda, 0.76 \sqrt{\frac{\hat{k}}{N^2}} \right) & N^2 > 0 \\ \Lambda & N^2 \leq 0 \end{cases} \quad (2.36)$$

Here Λ is the characteristic length scale,

$$\Lambda = (\Delta x \Delta y \Delta z)^{\frac{1}{3}} f(a_1, a_2) \quad (2.37)$$

$$f(a_1, a_2) = \cosh \left\{ \left[\frac{4}{27} (\ln^2 a_1 - \ln a_1 \ln a_2 + \ln^2 a_2) \right]^{\frac{1}{2}} \right\} \quad (2.38)$$

$$a_1 = \frac{\Delta_1}{\Delta_3}, \quad a_2 = \frac{\Delta_2}{\Delta_3}, \quad \Delta_1 \leq \Delta_2 \leq \Delta_3 \quad (2.39)$$

Δ_i is one of Δx , Δy and Δz . With the parameters mentioned above, we can compute C_ϵ in the following way,

$$C_\epsilon = 1.9C_s + (0.93 - 1.9C_s) \frac{\lambda}{\Lambda}, \quad C_s = 0.15 \quad (2.40)$$

Now we are able to calculate the eddy-viscosity coefficients. However, they have different formulas which depend on the stability of the PBL. So we here introduce Richardson number Ri and critical Richardson number Ri_c to represent different conditions of the PBL,

$$Ri = \frac{N^2}{S \cdot \Omega} \quad (2.41)$$

$$Ri_c = 0.25 \quad (2.42)$$

In general, there are three ordinary kinds of stability conditions in the PBL. For these three conditions we have different formulas for ν_m and ν_h as follows,

1. Unstable condition when $Ri < 0$,

$$\nu_m = \phi_m \lambda \sqrt{\hat{k}} \quad (2.43)$$

$$\nu_h = \phi_m \lambda \sqrt{\hat{k}} / Pr \quad (2.44)$$

$$\phi_m = \frac{C_s^{4/3} C_{eps}^{1/3} F_m^{2/3}}{\left(1 - \frac{Ri}{Pr}\right)^{1/3}} \quad (2.45)$$

$$Pr = \frac{F_m}{F_h} \quad (2.46)$$

$$F_m = (1 - 16Ri)^{\frac{1}{2}} \quad (2.47)$$

$$F_h = (1 - 40Ri)^{\frac{1}{2}} / Pr_N \quad (2.48)$$

2. Stable condition when $0 \leq Ri \leq Ri_c$

$$\nu_m = \phi_m \lambda \sqrt{\hat{k}} \quad (2.49)$$

$$\nu_h = \phi_m \lambda \sqrt{\hat{k}} / Pr \quad (2.50)$$

$$\phi_m = \frac{C_s^{4/3} C_{eps}^{1/3} F_m^{2/3}}{\left(1 - \frac{Ri}{Pr}\right)^{1/3}} \quad (2.51)$$

$$Pr = \frac{F_m}{F_h} \quad (2.52)$$

$$F_m = \left(1 - \frac{Ri}{Ri_c}\right)^4 \quad (2.53)$$

$$F_h = \left(1 - \frac{Ri}{Ri_c}\right)^4 \cdot \frac{1 - 1.2Ri}{Pr_N} \quad (2.54)$$

3. Very stable condition when $Ri > Ri_c$

$$\nu_m = \nu_{min} \quad (2.55)$$

$$\nu_h = \nu_{min} \quad (2.56)$$

$$\phi_m = 0 \quad (2.57)$$

$$Pr = 0 \quad (2.58)$$

$$Fm = 0 \quad (2.59)$$

$$Fh = 0 \quad (2.60)$$

Here C_{eps} is a constant, Pr_N is the Prandtl number for the neutral condition of the PBL,

$$C_{eps} = 0.93 \quad (2.61)$$

$$Pr_N = 0.7 \quad (2.62)$$

ν_{min} is the minimum value for ν_m and ν_h , it is set to $10^{-5}\text{m}^2/\text{s}$ in this study.

2.5 Canopy parameterization methods

2.5.1 Canopy terms for momentum equations

Forest canopies have many effects on the air flow in the PBL. First, they produce physical drag by the interaction of air flow and canopy elements. Moreover, canopies exchange heat and water vapor with surrounding air, which influences the temperature and humidity of the environment. Here we only consider the physical drag effect of the forest canopy. The drag term can be added into the momentum equations as follows [Shaw and Shumann (1992); Shen and Leclerc (1997); Finnigan (2000); Sogachev et al. (2002); Yue et al. (2007); Dupont and Brunet (2008); Gavrilov et al. (2011); Belcher et al. (2012); Edburg et al. (2012)],

$$\frac{\partial(\bar{\rho}\hat{u}_i)}{\partial t} + \frac{\partial}{\partial x_j}(\bar{\rho}\hat{u}_i\hat{u}_j) = -\frac{\partial\bar{p}}{\partial x_i} - 2\bar{\rho}\epsilon_{ijk}\Omega_j\hat{u}_k + \bar{\rho}g_i - \frac{\partial\tau_{ij}}{\partial x_j} - \bar{\rho}C_dA\hat{U}\hat{u}_i \quad (2.63)$$

The last term expresses the canopy drag, in which \hat{U} is the time-averaged (in the RANS model) or resolved (in the LES model) wind speed,

$$\hat{U} = \sqrt{\hat{u}^2 + \hat{v}^2 + \hat{w}^2} \quad (2.64)$$

A is taken as the frontal area density [Sogachev et al. (2002); Yue et al. (2007); Dupont and Brunet (2008)], which can be simply calculated as,

$$A = 0.5\text{LAD}(x, y, z) \quad (2.65)$$

Here LAD refers to Leaf Area Density, which describes the leaf surface area in a unit volume. C_d is the drag coefficient, it is usually set to a constant value. In this thesis we set C_d as 0.15 [Shaw and Shumann (1992); Gavrilov et al. (2011)].

From the expression of the canopy term we can find that the canopy drag force is always opposite to the momentum, indicating a decrease of the absolute value of momentum.

2.5.2 Canopy terms for the RANS model

Canopy drag not only affects the momentum but also the production and dissipation of TKE. Following the method used in Sogachev (2009), we can rewrite the $k - \epsilon$ equations with canopy terms as follows,

$$\frac{\partial}{\partial t}(\bar{\rho}\hat{k}) + \frac{\partial}{\partial x_j}(\bar{\rho}\hat{u}_j\hat{k}) = \frac{\partial}{\partial x_j} \left(\frac{\bar{\rho}\nu_m}{\sigma_k} \frac{\partial \hat{k}}{\partial x_j} \right) + P - \bar{\rho}\hat{\epsilon} + B \quad (2.66)$$

$$\begin{aligned} \frac{\partial}{\partial t}(\bar{\rho}\hat{\epsilon}) + \frac{\partial}{\partial x_j}(\bar{\rho}\hat{u}_j\hat{\epsilon}) &= \frac{\partial}{\partial x_j} \left(\frac{\bar{\rho}\nu_m}{\sigma_\epsilon} \frac{\partial \hat{\epsilon}}{\partial x_j} \right) + C_{1\epsilon} \frac{\hat{\epsilon}}{\hat{k}} P - C_{2\epsilon} \bar{\rho} \frac{\hat{\epsilon}^2}{\hat{k}} \\ &+ \frac{\hat{\epsilon}}{\hat{k}} [(C_{1\epsilon} - C_{2\epsilon})(B - S_d)] \end{aligned} \quad (2.67)$$

Here B is the buoyancy effect on TKE,

$$B = -\bar{\rho}\nu_h N^2 \quad (2.68)$$

$$\nu_h = \frac{\nu_m}{Pr_t} \quad (2.69)$$

It can be ignored in neutral boundary layer. In stable condition, the negative buoyancy term reduces TKE. At the same time, the buoyancy term is positive for ϵ . The

increase of dissipation decreases TKE as well. So the turbulence is suppressed in a stable PBL. While in unstable condition, B is positive for TKE and negative for dissipation, leading to increase of TKE. Pr_t is the turbulent Prandtl number, which is usually in the range from 0.7 to 0.9. In our research we use the value of 0.85.

S_d is the dissipation of TKE by the interaction of the air flow with the canopy elements.

$$S_d = 12\bar{\rho}C_\mu^{1/2}C_dA\hat{U}\hat{k} \quad (2.70)$$

$$C_\mu = 0.09 \quad (2.71)$$

S_d is always positive, so it has an increasing effect of dissipation and thus decreases TKE. This term is directly related to the canopy drag, so the existence of canopies usually reduces TKE.

2.5.3 Canopy terms for the LES model

In the LES model, we also need to add an additional term for the canopy drag [Shaw and Shumann (1992); Gavrilov et al. (2011)],

$$\begin{aligned} \frac{\partial}{\partial t}(\bar{\rho}\hat{k}) + \frac{\partial}{\partial x_j}(\bar{\rho}\hat{u}_j\hat{k}) = \frac{\partial}{\partial x_j} \left(\bar{\rho}\nu_m \frac{\partial \hat{k}}{\partial x_j} \right) + P + B - C_\epsilon \frac{\bar{\rho}\hat{k}^{3/2}}{\lambda} \\ - 2\bar{\rho}C_dA\hat{U}\hat{k} \end{aligned} \quad (2.72)$$

Similarly, the canopy drag decreases TKE as well in the LES model.

3

Methods

3.1 Introduction

In this chapter we will show the configurations of the simulations, which includes the domain size, the grid size, boundary conditions, initial conditions, canopy profile and so on.

3.2 Numerical method

Our simulations are performed with ASAM, which uses the Finite Volume Method (FVM) for spatial discretization and implicit time integration scheme. Following the numerical method in Shaw and Shumann (1992), the computation domain is set to $192 \times 96 \times 60\text{m}$ in the x , y and z directions. The grid size in each direction is 2m. ASAM uses the FVM, so the output data are all obtained from the centers of grid cells. Therefore, the lowest layer is 1m high from the ground. For this study, the forest canopy is horizontally homogeneous and its height h is 20 m. The vertical profile of LAD is shown in Figure 3.1, which represents a deciduous forest. The leaf area index (LAI) for this case is 5. The LAD profile in Shaw and Shumann (1992) is also given for comparison [Figure 3.2].

The time step is 0.1 s which is small enough to keep the computation stable. For a 10-minute simulation, the computation should proceed for 6000 time steps.

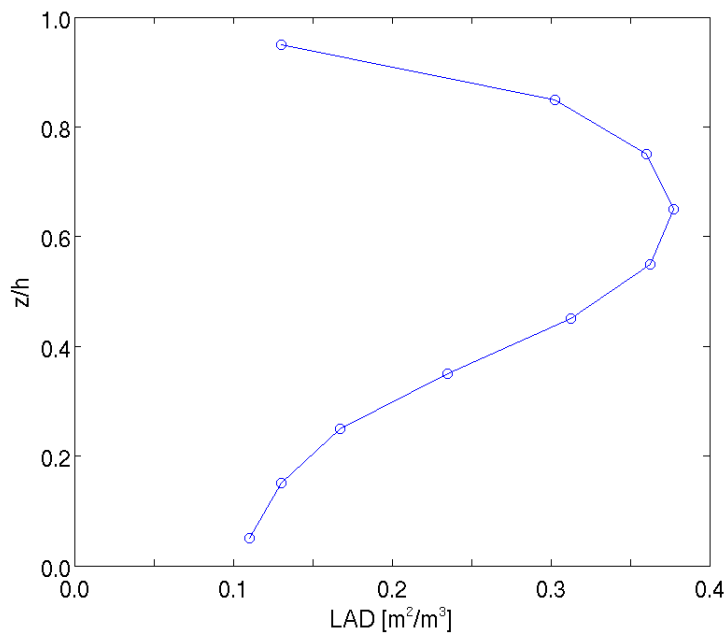


Figure 3.1: Vertical profile of LAD, the height is normalized by the canopy height.

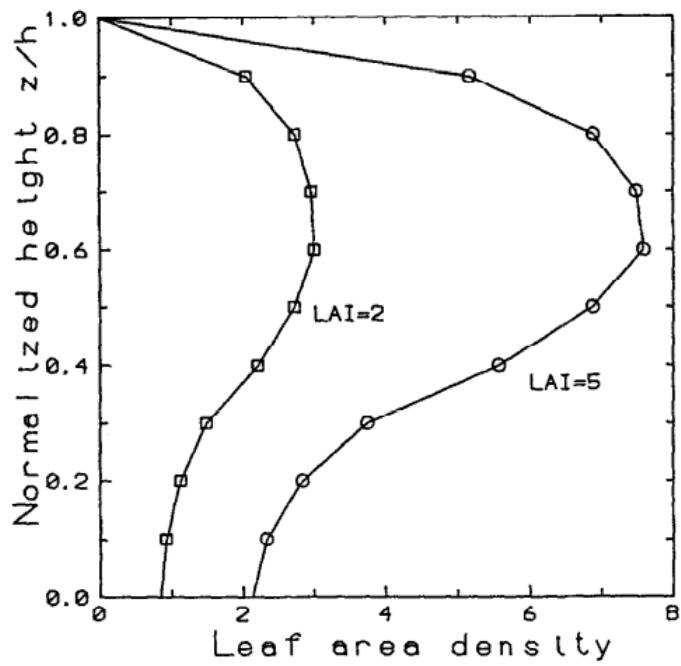


Figure 3.2: Fig. 2 in Shaw and Shumann (1992), Vertical profile of LAD, the height is normalized by the canopy height and the LAD is multiplied by the canopy height.

The test cases were all run in the supercluster of CSC with 32 cpus, each test run consumed about 2 hours.

The lateral boundaries are periodic. The upper boundary is set to free-slip. No-slip condition is used in the lower boundary. Moreover, the Louis scheme [Louis (1979)] is applied in the lowest layer for calculating the drag force of the roughness ground surface. The roughness length here is 0.02 m.

Following the numerical method in Shaw and Shumann (1992), the initial fields of u , v , w and TKE were set to uniform, but small perturbations were added to generate three-dimensional motions. Here u refers to the x component of velocity, corresponding to the longitudinal velocity in Shaw and Shumann (1992). v represents the horizontal velocity in y direction and w is the vertical velocity. The uniform values of u , v , w and TKE were 2 m/s, 0 m/s, 0 m/s and $0 \text{ m}^2/\text{s}^2$, respectively. For the RANS model, the dissipation rate of TKE ϵ was set to $0 \text{ m}^2/\text{s}^3$ within the computational domain without perturbations. In Shaw and Shumann (1992), three kinds of PBL were examined, but only the results of neutral stability and weakly convective conditions were shown. So here we only simulated these two kinds of PBL. For the neutral condition, the initial values of potential temperature were set to 289.0 K in the whole domain with small perturbations. While in the weakly convective case, the potential temperature was taken as 289.0 K inside the canopy and linearly decreased above it at a rate of 0.025 K/m.

Coriolis force was excluded in Shaw and Shumann (1992) due to its little contribution. In this study, we will also remove it to get the results for comparison.

4

Results and discussion

4.1 Introduction

Using the formulas derived in chapter 2, we implemented the canopy parameterization methods in ASAM for the RANS model and the LES model, separately. In this chapter we will run some test cases to verify the feasibility of the models with canopy parameterization. The benchmark for the numerical models refers to the cases used by Shaw and Shumann (1992). The results of the LES model are displayed and compared with that in Shaw and Shumann (1992) or with the observation data. After that, comparisons between the RANS model and the LES model are discussed.

4.2 Vertical profiles of spatially averaged fields

Shaw and Shumann (1992) showed some profiles of horizontally averaged fields, including u , the Reynolds stress, the TKE and the skewnesses of u and w under weakly unstable condition. These figures in Shaw and Shumann (1992) are also shown here for convenience. Here we will also illustrate the figures of these profiles for comparisons. In addition, the profiles of the normalized standard deviations of u , v and w , as well as the correlation coefficients between u and w are given for further discussion. The figures were plotted by Matlab and the data were obtained

from the LES model run under weakly convective condition.

Figure 4.1 shows the vertical profile of horizontally averaged u . The profile shape is very similar to that in Shaw and Shumann (1992) [Figure 4.2] except the values are slightly larger. Both the near-logarithmic increasing above the canopy and the near-exponential decay in the upper part of the canopy are presented in Figure 4.1. The coupling parameter R_c , which is defined as the ratio of wind velocity at $z = 0.25h$ to that at $z = 1.4h$ [Shaw and Shumann (1992)], is 0.29. This value is very close to the R_c (0.26) for LAI=2 in Shaw and Shumann (1992). The probable reason of it is: Shaw and Shumann (1992) used local foliage density a in the canopy drag terms which is equivalent to LAD, but in this study we used frontal area density A instead which is half of LAD. In the following comparisons and discussions, we will still use the results with A . A difference also exists for the lowest point because in ASAM the data are saved in the centers of grid cells. So the profile does not contain the velocity at the ground.

The horizontally averaged v and w are almost zero in each layer which are not shown here.

The Reynolds stress are shown in Figure 4.3. It is calculated in each layer using this spatially averaging formula,

$$Rs = -\overline{u'w'} \quad (4.1)$$

which indicates that for a positive vertical gradient of u , Rs is normally larger than zero. The square root of the absolute value of the Reynolds stress at the top of the canopy is noted as u_* ,

$$u_* = \sqrt{|\overline{u'w'}|} \Big|_{z=h} \quad (4.2)$$

Here $u_* = 0.25$ m/s under weakly unstable condition.

The profile shown here is also in good agreement with that in Shaw and Shumann (1992) [Figure 4.4]. It decreases rapidly inside the forest due to the canopy drag, and also decays above the canopy approximately linearly in average. We should notice that in the lower part of the canopy ($z < 0.5h$), the vertical gradient of u is negative, so the Reynolds stress should be also negative. However, the Reynolds stress is

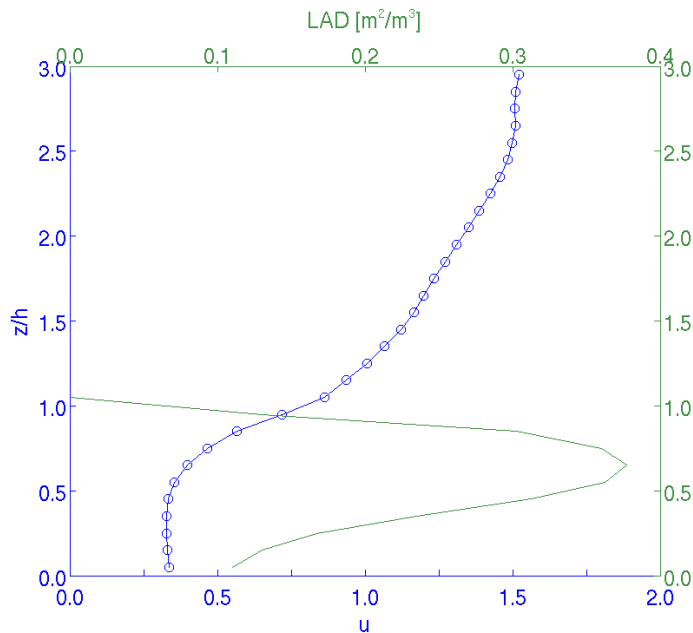


Figure 4.1: Vertical profile of horizontally averaged u (blue solid line with open circles) under weakly unstable conditions for the LES model. The profile of LAD is superimposed as well (green solid line), the same below. The height is normalized by the canopy height and u is normalized by the vertically averaged u ($=1.04$ m/s in this LES model run).

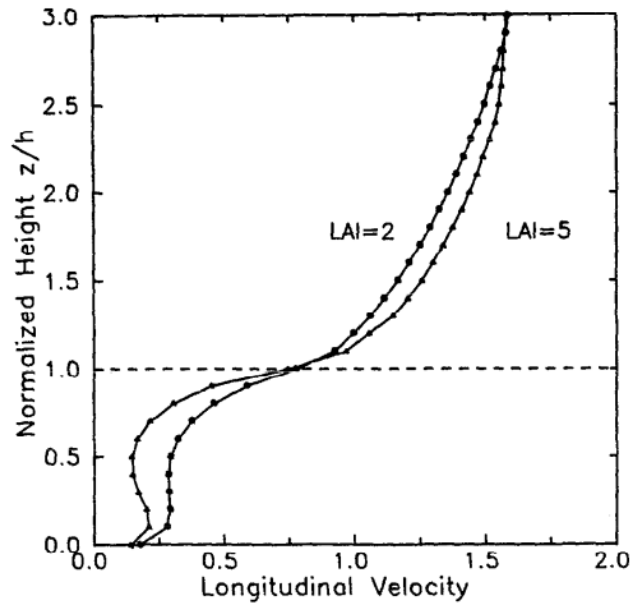


Figure 4.2: Fig. 3 in Shaw and Shumann (1992), vertical profile of horizontally averaged u for LAI=2 and LAI=5 under weakly unstable conditions. The height is normalized by the canopy height and u is normalized by the vertically averaged u .

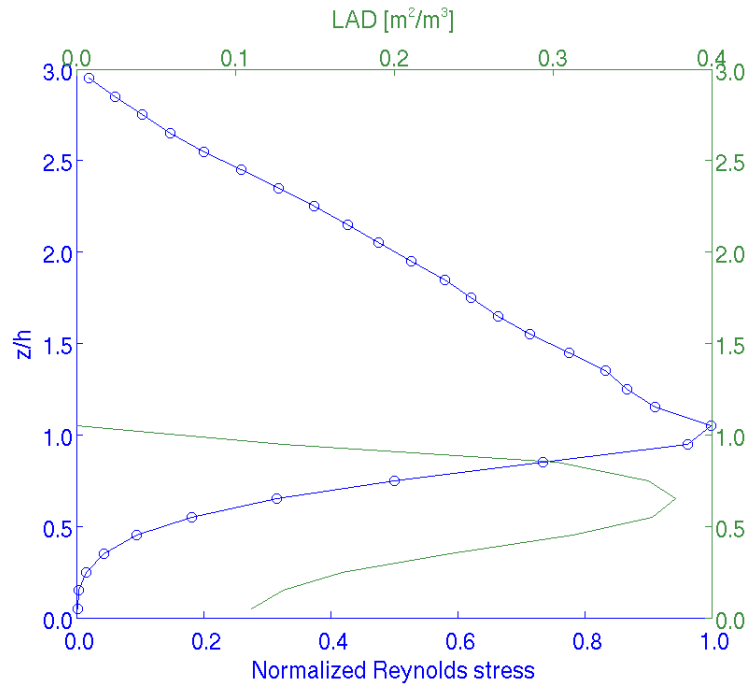


Figure 4.3: Vertical profile of the normalized Reynolds stress under weakly unstable condition for the LES model. The stress is normalized by its value at the top of the canopy.

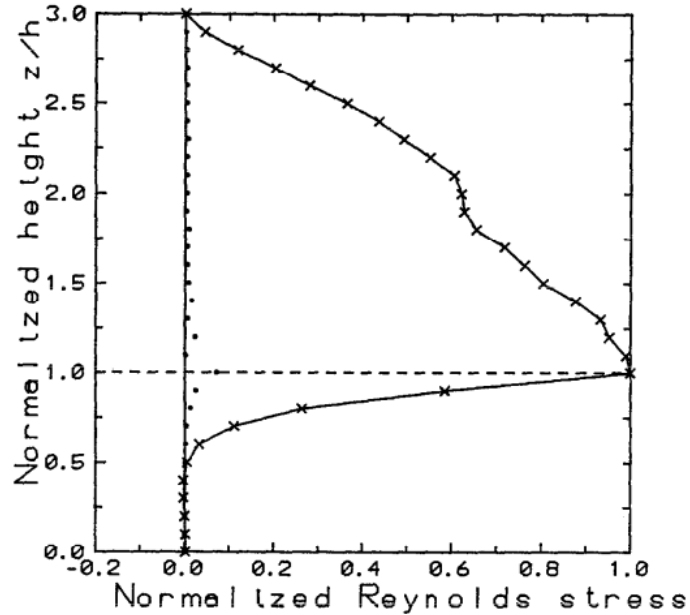


Figure 4.4: Fig. 4 in Shaw and Shumann (1992), same as Figure 4.3. The dots are subgrid-scale (SGS) component of the Reynolds stress and the solid line is the sum of resolved and SGS components.

larger than zero at any height. Therefore, in this region turbulences transport the horizontal momentum from low-value area to high-value area. This kind of momentum flux is called counter-gradient flux, which was also found in Shaw and Shumann (1992). The difference between the result in our simulation and in Shaw and Shumann (1992) is that Rs starts to grow from the near ground here, while the Reynolds stress just keeps almost zero below $z = 0.5h$ in Shaw and Shumann (1992) [Figure 4.4].

We should also notice that the decreasing of the Reynolds stress above the canopy is inconsistent with the observed data [Finnigan (2000)], which may be due to the limited domain height and the free-slip upper boundary. This was also mentioned in Shaw and Shumann (1992).

Figure 4.5 gives the profiles of resolved and subgrid-scale (SGS) components of TKE. Again, the shapes and tendencies are similar with that in Shaw and Shumann (1992) [Figure 4.6]. The resolved TKE decreases quickly inside the canopy due to the canopy drag. It reaches its maximum value just on the top of the canopy, and decays from about 2.3 to around 1.0 at the top of the domain. The SGS TKE is calculated by the extra equation for parameterization [Equation 2.72]. Its maximum values are also on the top of the canopy, but are only 3% to 5% of the resolved ones. In Shaw and Shumann (1992), the percentage is about 10%. It should be noted that the values of TKE are much smaller than that in Shaw and Shumann (1992) if we use the same normalization method since u is about 4 times as u_* . However, if normalized by u_*^2 our TKE values are consistent with the variances of wind speed components, see Figure 4.9 below. In fact, the TKE can be calculated from the standard deviations of wind velocity as follows,

$$\text{TKE} = (\sigma_u^2 + \sigma_v^2 + \sigma_w^2)/2 \quad (4.3)$$

where σ_u , σ_v and σ_w are the standard deviations of u , v and w , respectively. Thus we believe that Shaw and Shumann (1992) have presented their TKE profiles with a different normalization method, for example, the TKE is normalized by the squared friction velocity at the canopy top (i.e. u_* here) as what we have done here [see also Massman and Weil (1999)].

Similarly as the Reynolds stress, the profile of the resolved TKE shown here is in disagreement with the observations. In observations the TKE remains constant or increases slightly above the canopy. Likewise, the limited domain height and free-slip upper boundary suppress the production of TKE [Shaw and Shumann (1992)].

The third-order moments of three components of velocity are also plotted [Figure 4.7]. Here we calculate the skewness of u in each layer using the spatially averaging formula,

$$Sk_u = \frac{\overline{u'^3}}{\sigma_u^3} \quad (4.4)$$

Where σ_u is the standard deviation of u . The skewnesses of v and w can be obtained in the same manner.

From Figure 4.7 we can see that the skewness of u is negative near the ground but becomes positive in the other part within the canopy layer. Its shape inside the canopy is following the profile of LAD but is slightly wider. The profile of the skewness of u inside the canopy is not consistent with that in Shaw and Shumann (1992), where it keeps nearly constant within this region [Figure 4.8]. But the shape shown here is closer to the observed data [see Fig. 6 in Rannik et al. (2003)]. Above the canopy the skewness decreases to its minimum value at about $z = 2.1h$, then it increases till the top in average. The average value of the skewness of u above the canopy is nearly the same as that in Shaw and Shumann (1992), but the profile here shows much larger variation.

w is skewed negatively from the ground to the top of the canopy with the minimum value at about $z = 0.5h$, then the skewness of w increases somewhat to its maximum value 0.3 at the top of the domain. Inside the canopy the profile is in good agreement with that in Shaw and Shumann (1992). While in the upper part of the domain, the skewness does not change much which is not consistent with that in Shaw and Shumann (1992). But it fits the observed data much better [see Fig. 6 in Rannik et al. (2003)].

The skewness of v only changes slightly through the whole domain with the average value of about 0.03.

The profiles of normalized standard deviations of u , v and w are also plotted

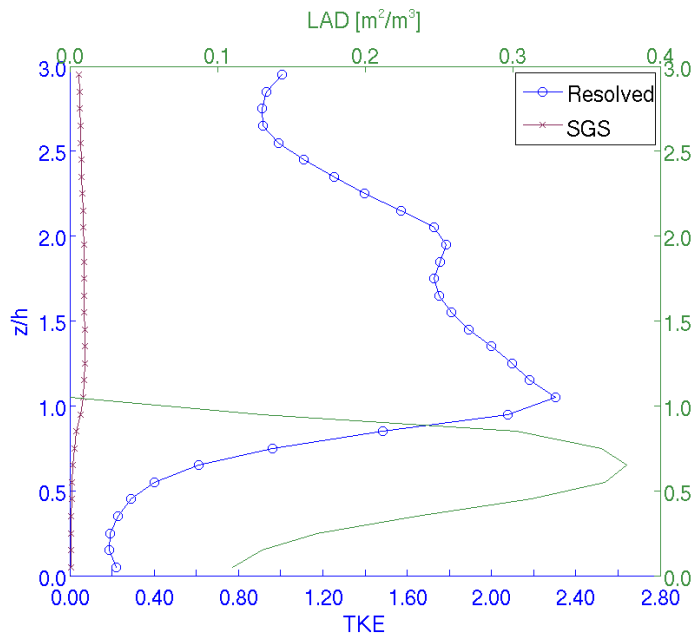


Figure 4.5: Vertical profiles of the resolved (blue solid line with open circles) and SGS (red solid line with crosses) components of the TKE under weakly unstable condition for the LES model. The TKE values are normalized by the square of u_* .

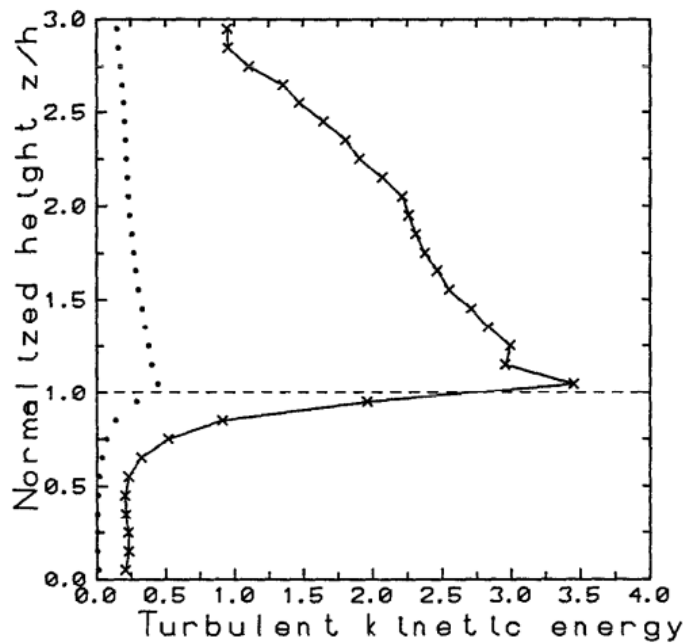


Figure 4.6: Fig. 6 in Shaw and Shumann (1992), Same as Figure 4.5 but the dots are SGS component of TKE and the solid line is the sum of resolved and SGS components. Here the TKE values are normalized by the square of vertically averaged u .

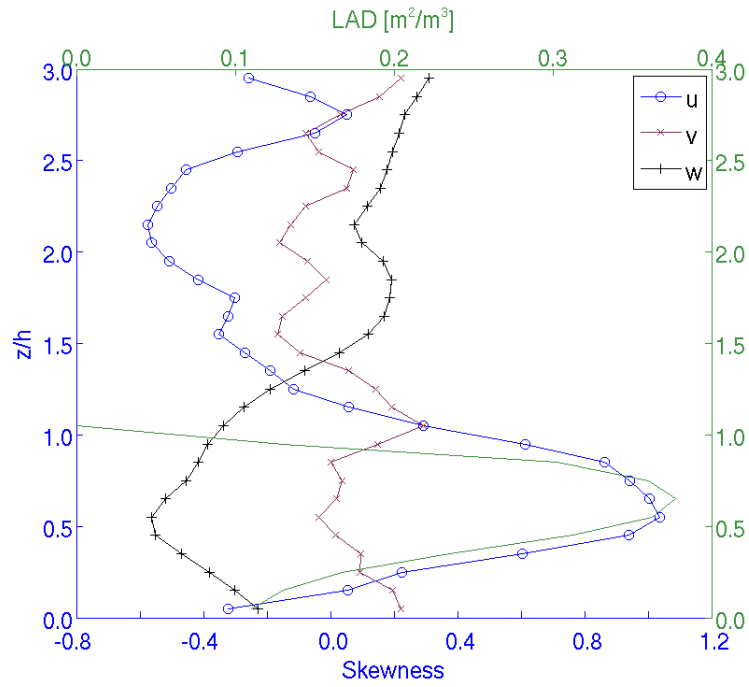


Figure 4.7: Vertical profiles of the skewnesses of u (blue solid line with open circles), v (red solid line with crosses) and w (black solid line with plus symbols) under weakly unstable condition for the LES model.

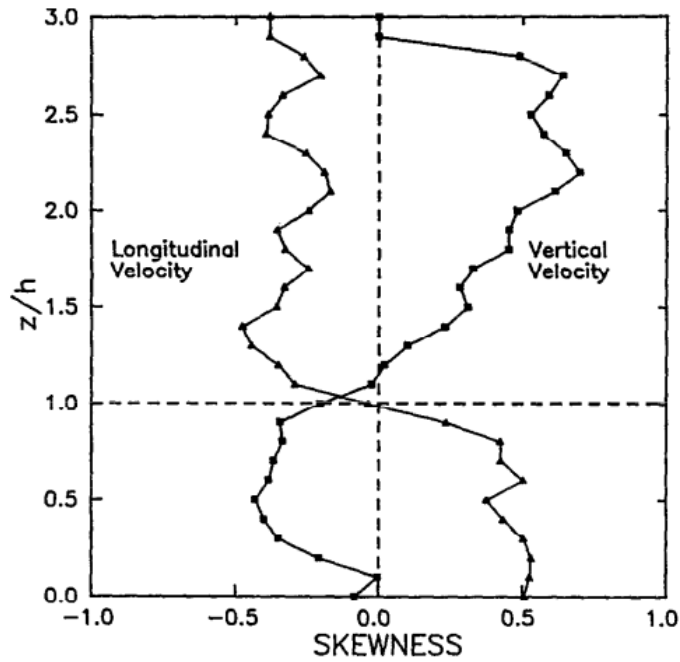


Figure 4.8: Fig. 7 in Shaw and Shumann (1992), same as Figure 4.7 but only for skewnesses of u and w .

[Figure 4.9] which are not given in Shaw and Shumann (1992). The profiles of u and v have similar shapes. Both of them keep nearly constant in the lower part of the canopy, then they increase rapidly to their maximum values at (for u) or above (for v) the top of the canopy. In the upper part of the domain, the normalized standard deviations of u and v decrease till approximately $z = 2.5h$. Then they increase until the top. The profile for w is also similar with the other two except that it increases rapidly within the whole canopy as well as continuously decreases above the forest.

Some studies showed the observed data for the profiles of normalized standard deviations of velocity [Massman and Weil (1999); Finnigan (2000); Rannik et al. (2003)]. The results of our simulation are in good agreement with the observations qualitatively. But two differences should be noted here. First, take the normalized standard deviation of u for example, the observed values vary from about 0.55 near the surface to around 2.27 above the canopy [see Table II in Rannik et al. (2003)]. Similar values can also be found in Massman and Weil (1999). In our simulation the corresponding values are about half of the observed ones but have the same magnitude. Similar differences exist for v and w as well. Secondly, the profiles of observations nearly keep constant above the canopy. However, both differences are reasonable since the limited domain height has suppressed the development of turbulence and the rigid upper boundary has decreased the fluctuations of velocity in the upper part.

Figure 4.10 shows the profile of correlation coefficients between u and w which is noted as r_{uw} . The absolute value of r_{uw} can represent how efficiently the horizontal momentum can be transported in the vertical direction [Finnigan (2000)]. From the figure we can see that it is nearly zero near the ground, where the Reynolds stress is also zero. Then r_{uw} decreases rapidly to its minimum value, around -0.7, at around $z = 0.8h$. The height of the minimum point is a little larger than the result in Rannik et al. (2003), but is consistent with the result in Finnigan (2000). It should be noted that the LAD profile used in Rannik et al. (2003) is slightly different from that in our simulations. This may cause some differences. However, the minimum value of r_{uw} is larger than the observations, but it is still within the error range [see Fig. 4 in Rannik et al. (2003)].

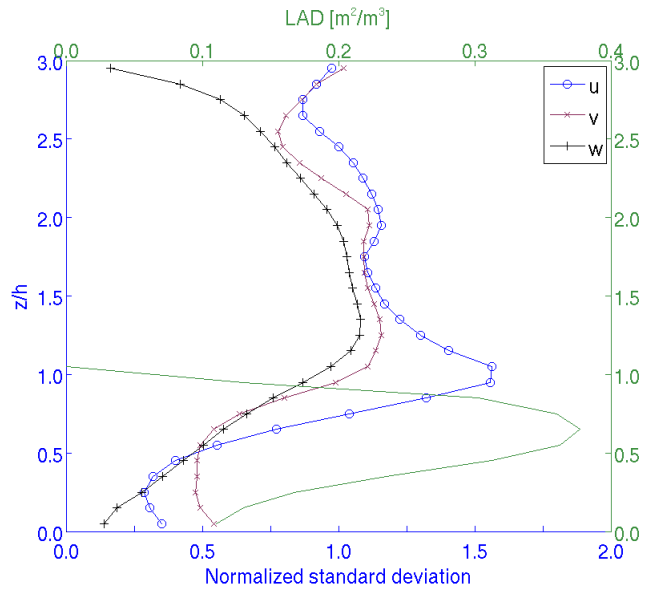


Figure 4.9: Vertical profiles of the standard deviations of u (blue solid line with open circles), v (red solid line with crosses) and w (black solid line with plus symbols) under weakly unstable condition for the LES model. The values are normalized by u_* .

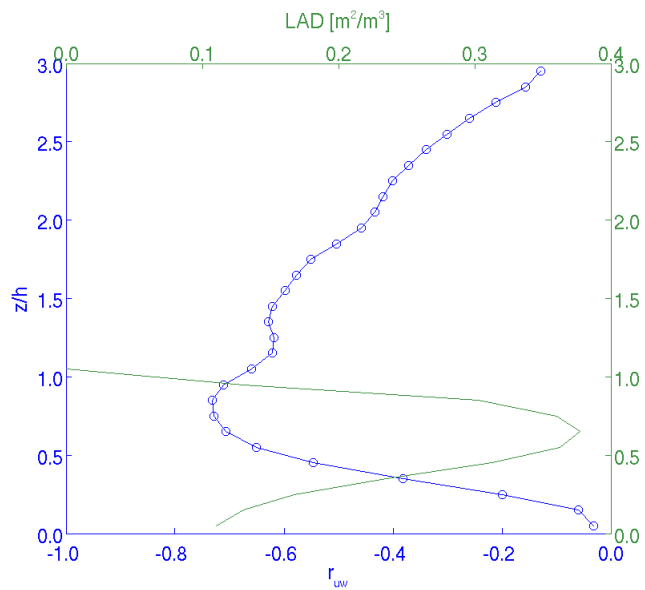


Figure 4.10: Vertical profile of the correlation coefficients between u and w under weakly unstable condition for the LES model.

In the upper domain, observations show nearly constant r_{uw} values, about -0.3 to -0.5, till the top [Finnigan (2000); Rannik et al. (2003)]. However, due to the effects of the limited domain height and the rigid upper boundary, r_{rw} increases quickly to about 0.1 near the top of the domain. But the average value of r_{uw} in the range of $z = 1.0h$ to $z = 2.5h$ is about 0.5, which is similar with the observations.

From the figures and discussions above we can find that the results of our simulations are in good agreement with that in Shaw and Shumann (1992). The profiles of standard deviations of velocity and r_{uw} are also shown to be qualitatively consistent with the results of the observations. So the LES model we used for this study is reliable to predict the essential features of turbulent statistics. Moreover, the method we used to generate weakly unstable boundary layer is proved feasible.

4.3 Cross sections of instantaneous fields

For a 3-dimensional (3D) case, plotting slice contours at specific cross sections are a good way to reveal the characteristics of the turbulent flow. So in this section we will show some contour figures of cross sections.

In Shaw and Shumann (1992), the instantaneous fields were obtained from the simulation under neutral condition. So for comparisons we will also use the data of the simulation for the neutral boundary layer. Figure 4.11 gives an example of instantaneous u field in the x - z cross section at $y = 2.35h$. The slice shows that u normally increases with height except some regions near the ground. This is consistent with the result of the profile of u in section 4.2. The vertical shear of u varies in x direction and the shear is largest at $x = 0.0h$. Since the flow is periodic in horizontal directions, it is the same at $x = 9.6h$ as $x = 0.0h$. Also, the shear have other two regions with large values near the canopy top, one is at about $x = 1.3h$ and the other one is at $x = 4.8h$. While inside and above the canopy the values of the vertical shear are much smaller.

The contour plot of w is shown in Figure 4.13. Three downdraft regions as well as three updraft regions can be observed in the figure. Compared to Figure 4.11, we can find that the downdraft regions are very close to the sharp u gradient areas. In

contrary, the updraft regions are associated with the weak shear areas. The coupled patterns between u and w can be also seen from the vector field [Figure 4.15]. For example, three wavy patterns near the top of the forest canopy are much clearer in the figure. However, the wavy patterns are not obvious in Figure 4.16. Although the coupled regions are not in the same places as that in Shaw and Shumann (1992), the coherent relationship between u and w are revealed quite well by our simulation [Figure 4.12 and Figure 4.14].

Since in this study we do not consider the effects of the forest canopy on the heat flux, the contour plots for the temperature fluctuation and patterns shown as Fig. 11 and Fig. 12 in Shaw and Shumann (1992) are not plotted here.

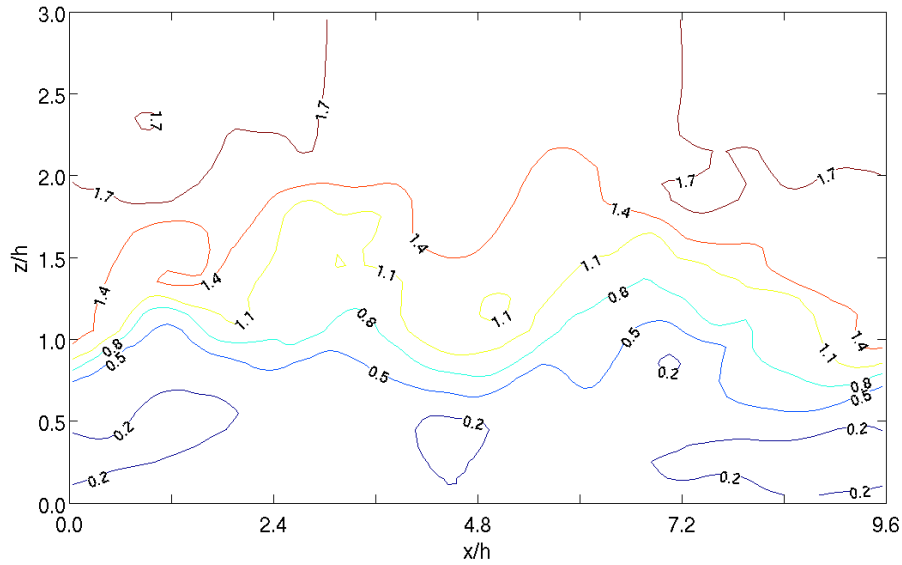


Figure 4.11: Contour plot for u field on the x - z cross section at $y = 47$ m ($y = 2.35h$) under neutral condition for the LES model. u is normalized by the vertically averaged u . x and z coordinates are normalized by the canopy height. Contour interval is 0.3.

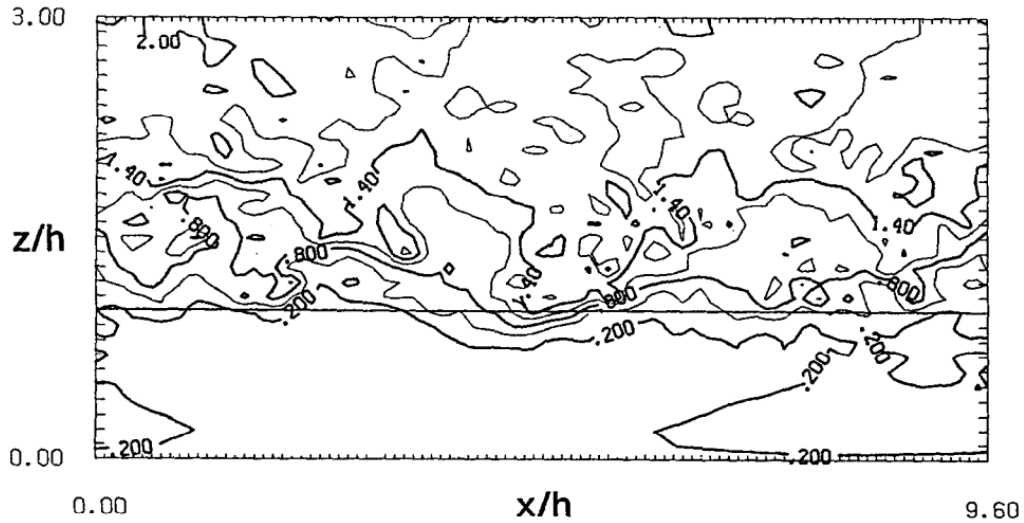


Figure 4.12: Fig. 8 in Shaw and Shumann (1992), same as Figure 4.11 but the slice is at $y = 2.4h$.

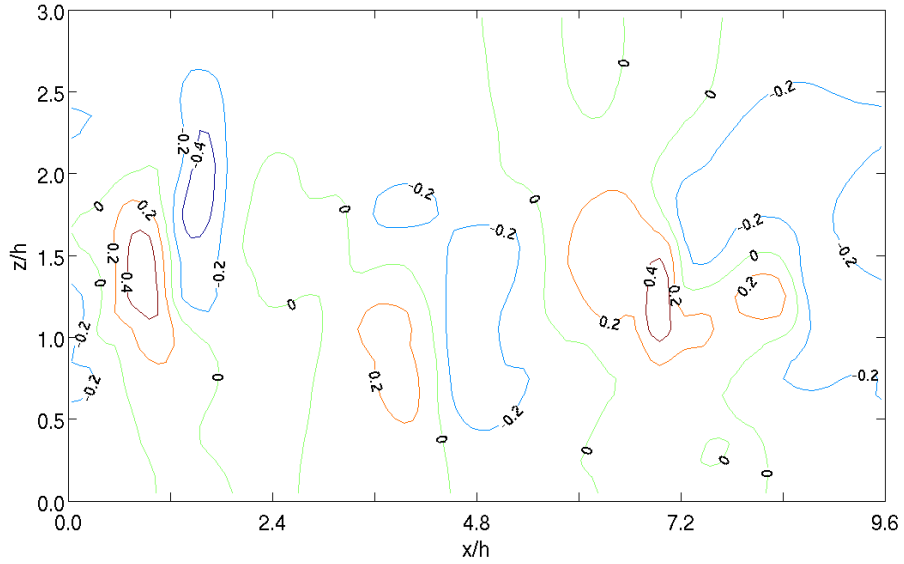


Figure 4.13: Contour plot for w field on the x - z cross section at $y = 47$ m ($y = 2.35h$) under neutral condition for the LES model. w is normalized by the vertically averaged u . x and z coordinates are normalized by the canopy height. Contour interval is 0.2.

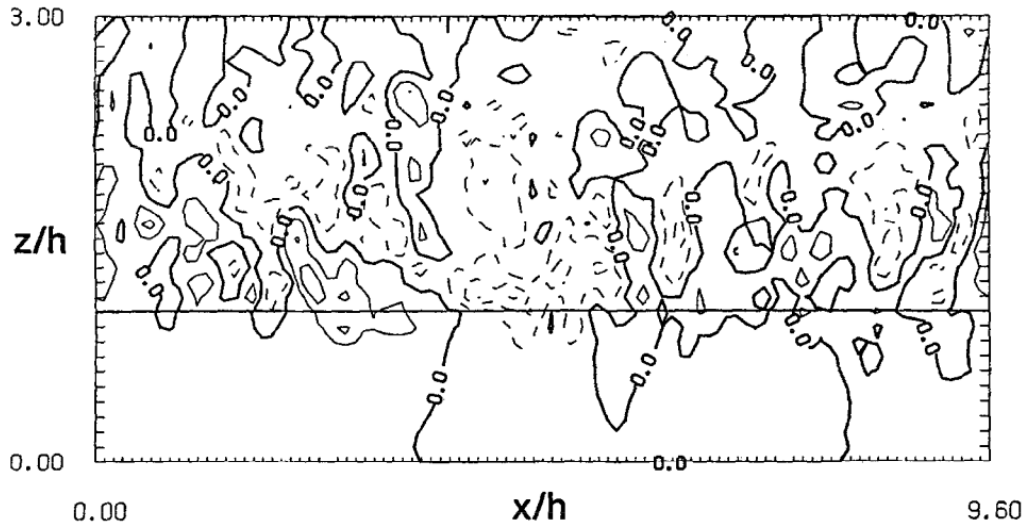


Figure 4.14: Fig. 9 in Shaw and Shumann (1992), same as Figure 4.13 but the slice is at $y = 2.4h$.

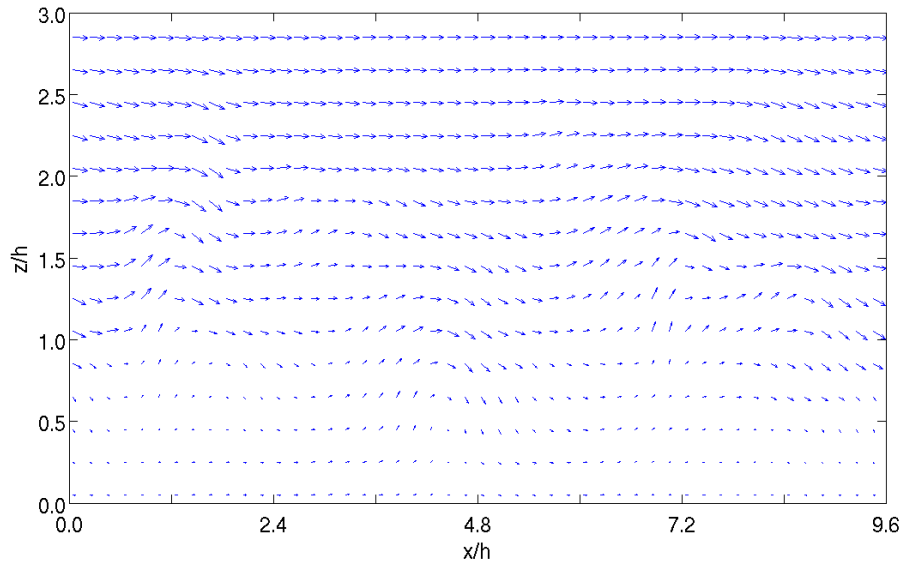


Figure 4.15: Velocity vector on the x-z cross section at $y = 2.35h$ under neutral condition for the LES model. x and z coordinates are normalized by the canopy height. w is enlarged by a factor of 1.6 relative to u .

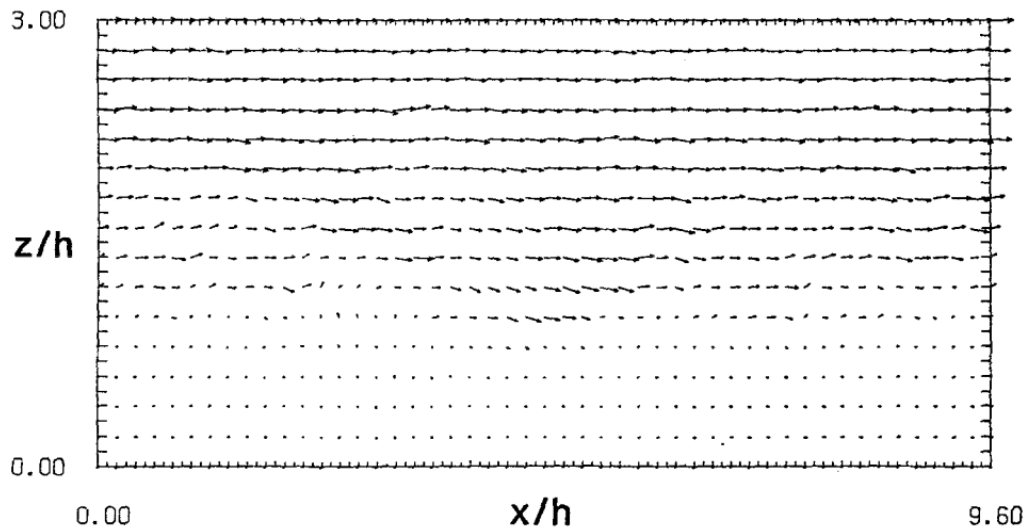


Figure 4.16: Fig. 10 in Shaw and Shumann (1992), same as Figure 4.15 but the slice is at $y = 2.4h$.

4.4 Results of the RANS model

In the last two sections we analyzed the results from the LES model, which showed good agreement with that in Shaw and Shumann (1992) as well as in observations and surely revealed many important features of the turbulent flow inside and above the forest canopy in the PBL. For comparison, the results of the RANS model under same conditions are given in this section. Figures 4.17 to 4.19 have shown the vertical profiles of u , the Reynolds stress and the TKE. A slice of time-averaged flow pattern is presented in Figure 4.20.

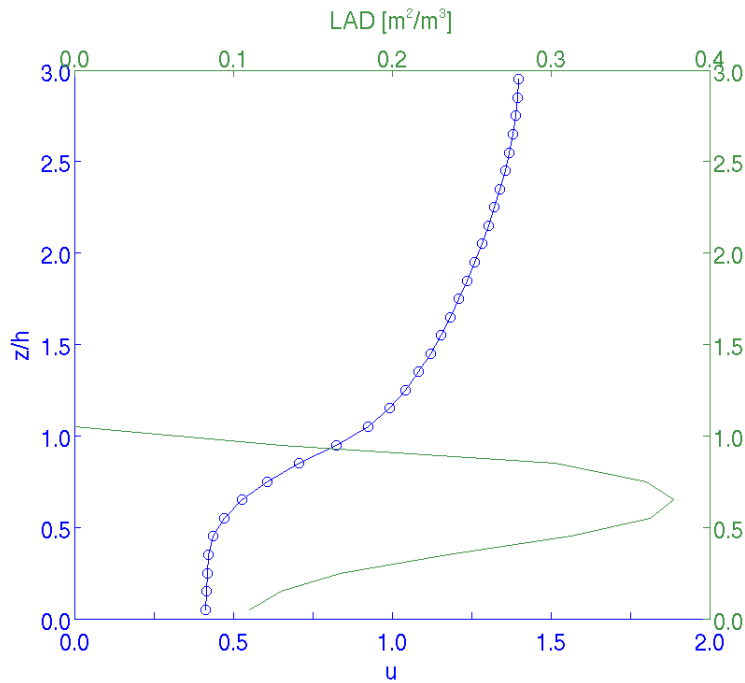


Figure 4.17: Vertical profile of horizontally averaged u under weakly unstable condition for the RANS model. The height is normalized by the canopy height and u is normalized by the vertically averaged u ($=0.96$ m/s in this RANS model run).

The u profile for the RANS model is nearly the same as that in the LES model, decreasing rapidly inside the canopy and revealing logarithmic shape above the canopy. However, it does not have a negative vertical gradient near the ground, which is an important characteristic for creating counter-gradient flux [Figure 4.17].

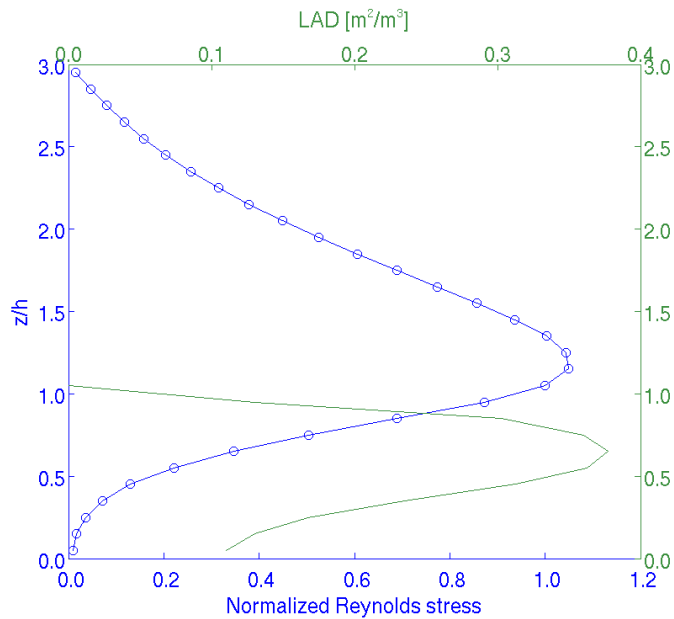


Figure 4.18: Vertical profile of the normalized Reynolds stress under weakly unstable condition for the RANS model. The stress is normalized by its value at the top of the canopy.

Here the profiles of horizontally averaged v and w are not shown, because in the RANS model the values of them are almost zero through the whole vertical direction as in the LES model.

The Reynolds stress also has a similar profile with that in the LES model. Again, time averaging makes it much smoother [Figure 4.18].

The TKE in the RANS model is obtained from the equation 2.66. Its vertical profile is shown in Figure 4.19. Here we normalized the TKE by the square of u_* ($u_* = 0.23$ m/s in this RANS model run). Although the observed data in Rannik et al. (2003) did not show the TKE profile directly, we can still calculate it from the normalized standard deviations of velocity by equation 4.3. So we can estimate the observed TKE values inside and above the canopy from Figure 4 and Table II in Rannik et al. (2003). The observations thus show that the TKE increases from about 0.3 near the surface to 4.9 above the canopy, and then keeps constant until the domain top. The results of our simulation are about 50% smaller but still show qualitative agreement with the measured data.

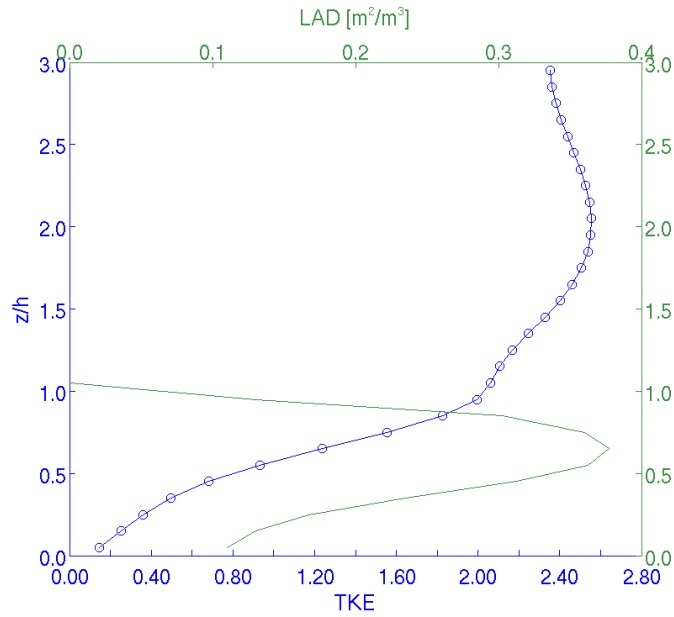


Figure 4.19: Vertical profile of the TKE under weakly unstable condition for the RANS model. The TKE values are normalized by the square of u_* .

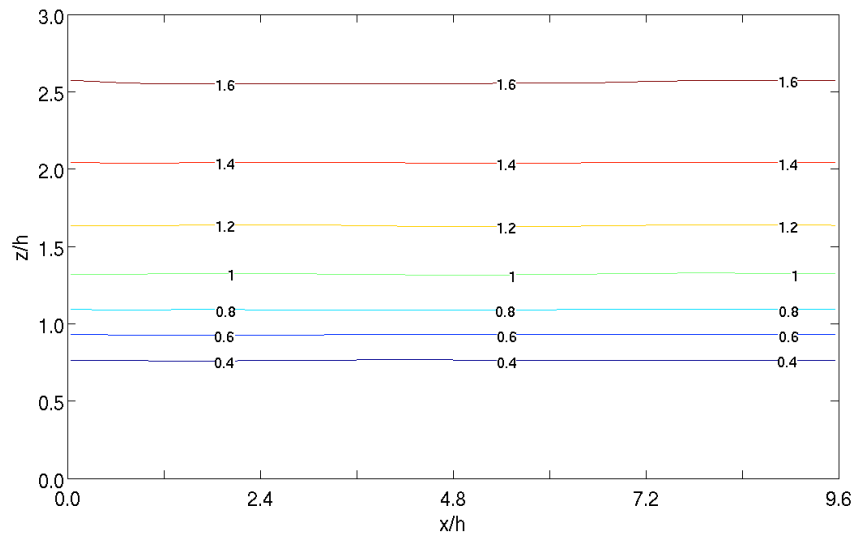


Figure 4.20: Contour plot for u field on the x - z cross section at $y = 47$ m ($y = 2.35h$) under neutral condition for the RANS model. u is normalized by the vertically averaged u . x and z coordinates are normalized by the canopy height. Contour interval is 0.2.

Figure 4.20 shows the cross section of the time-averaged u field under neutral condition for the RANS model. As we can expect, it is nearly horizontally homogeneous due to time averaging. This confirms the fact that the instantaneous turbulent flow cannot be revealed in the RANS model.

Overall, the RANS model is able to predict averaged fields and some turbulence statistics, for example, vertical profiles of u , Rs and TKE. However, it can not directly describe the turbulence. So it is not an appropriate tool for us to simulate the turbulent flow inside and above the canopy.



5

Conclusions

In this study, two parameterization methods for canopy have been added into ASAM, one is for the LES model and the other is for the RANS model. Then the numerical model ASAM is used to simulate the turbulent flow inside and above the forest canopy in the PBL with limited vertical extent.

The simulation results of the vertical profiles of mean flow and turbulence statistics for the LES model are presented and compared with the results in Shaw and Shumann (1992) and in some observations, showing good agreement with them. Therein, the counter-gradient flux in the lower part of the forest canopy is successfully predicted by the vertical profiles of u and Rs in our simulation. The flow patterns plotted with the instantaneous u and w fields are also listed. Although they do not match the results in Shaw and Shumann (1992) exactly due to the different closure equations and random initial conditions, the flow patterns of our simulation still correctly predicted the coupled relation between the downdraft regions and the areas with sharp vertical shear of u .

For comparison, the simulation results of the RANS model under the same conditions are also presented. The vertical profiles of u and Rs are similar with that in the LES model, and the TKE profile is consistent with the observations. However, the RANS model does not calculate the instantaneous turbulence field.

The simulation results mentioned above have already verified the feasibility of the canopy parameterization methods used in our study. We can also conclude that the LES model, rather than the RANS model, is an appropriate numerical tool to simulate the turbulent flow considering the effects of the forest canopy in the PBL.

Bibliography

- Arneth, A., N. Unger, M. Kulmala, and M. O. Andreae (2009). Clean the air, heat the planet. *Science* 326, 672–673.
- Aumond, P., V. Masson, C. Lac, B. Gauvreau, S. Dupont, and M. Berengier (2013). Including the drag effects of canopies: real case Large-Eddy Simulation studies. *Boundary-Layer Meteorol.* 146, 65–80.
- Belcher, S. E., I. N. Harman, and J. J. Finnigan (2012). The wind in the willows: flows in forest canopies in complex terrain. *Annual Review of Fluid Mechanics* 44(1), 479–504.
- Bonn, B., M. Kulmala, I. Riipinen, S.-L. Sihto, and T. M. Ruuskanen (2008). How biogenic terpenes govern the correlation between sulfuric acid concentrations and new particle formation. *J. Geophys. Res.* 113, D12209, doi:10.1029/2007JD009327.
- Boy, M., A. Sogachev, J. Lauros, L. Zhou, A. Guenther, and S. Smolander (2011). SOSA—a new model to simulate the concentrations of organic vapours and sulphuric acid inside the ABL – Part 1: Model description and initial evaluation. *Atmos. Chem. Phys.* 11, 43–51.
- Bryan, G. H. and J. M. Fritsch (2002). A benchmark simulations for moist nonhydrostatic numerical models. *Mon. Wea. Rev.* 130, 2917–2928.
- Bäck, J., J. Aalto, M. Henriksson, H. Hakola, Q. He, and M. Boy (2012). Chemodiversity of a Scots pine stand and implications for terpene air concentrations. *Biogeosciences* 9, 689–702.
- Dupont, S. and Y. Brunet (2008). Influence of foliar density profile on canopy flow: A large-eddy simulation study. *Agricultural and Forest Meteorology* 148(6-7), 976–990.
-

- Edburg, S. L., D. Stock, B. K. Lamb, and E. G. Patton (2012). The Effect of the Vertical Source Distribution on Scalar Statistics within and above a Forest Canopy. *Boundary-Layer Meteorol.* *142*(3), 365–382.
- Ehn, M., E. Kleist, H. Junninen, T. Petäjä, G. Lönn, S. Schobesberger, M. Dal Maso, A. Trimborn, M. Kulmala, D. R. Worsnop, A. Wahner, J. Wildt, and T. F. Mentel (2012). Gas phase formation of extremely oxidized pinene reaction products in chamber and ambient air. *Atmos. Chem. Phys.* *12*, 5113–5127.
- Filaus, E. (2007). Reibungsbehaftete Überströmung quasi-zweidimensionaler Hindernisse. Master’s thesis, Universität Leipzig & Leibniz-Institut für Troposphärenforschung.
- Finnigan, J. (2000). Turbulence in plant canopies. *Annu. Rev. Fluid Mech.* *32*, 519–571.
- Forster, P., V. Ramaswamy, P. Artaxo, T. Berntsen, R. Betts, D. W. Fahey, J. Haywood, J. Lean, D. C. Lowe, G. Myhre, J. Nganga, R. Prinn, G. Raga, M. Schulz, and R. Van Dorland (2007). *Changes in Atmospheric Constituents and in Radiative Forcing. In: Climate Change 2007: The Physical Science Basis. Contribution of Working Group I to the Fourth Assessment Report of the Intergovernmental Panel on Climate Change.* Cambridge University Press, Cambridge, United Kingdom and New York, NY, USA.
- Gavrilov, K., G. Accary, D. Morvan, D. Lyubimov, S. Méradji, and O. Bessonov (2011). Numerical simulation of coherent structures over plant canopy. *Flow, Turbulence and Combustion* *86*(1), 89–111.
- Guenther, A. B., X. Jiang, C. L. Heald, T. Sakulyanontvittaya, T. Duhl, L. K. Emmons, and X. Wang (2012). The Model of Emissions of Gases and Aerosols from Nature version 2.1 (MEGAN2.1): an extended and updated framework for modeling biogenic emissions. *Geosci. Model Dev.* *5*, 1471–1492.
- Hakola, H., V. Tarvainen, T. Laurila, V. Hiltunen, H. Hellén, and P. Keronen (2003).

- Seasonal variation of VOC concentrations above a boreal coniferous forest. *Atmos. Env.* *37*, 1623–1634.
- Haywood, J. and O. Boucher (2000). Estimates of the direct and indirect radiative forcing due to tropospheric aerosols: a review. *Reviews of Geophysics* *38*(4), 513–543.
- Haywood, J. and M. Schulz (2007). Causes of the reduction in uncertainty in the anthropogenic radiative forcing of climate between IPCC (2001) and IPCC (2007). *Geophysical Research Letters* *34*. L20701, doi:10.1029/2007GL030749.
- Herzog, H.-J., U. Schubert, G. Vogel, A. Fiedler, and R. Kirchner (2002). LLM - the high-resolving nonhydrostatic simulation model in the DWD - Project LITFASS (Part I: Modelling Technique and Simulation Method). *Technical Report No. 4*. Deutscher Wetterdienst, Offenbach, Germany.
- Hinneburg, D. and O. Knoth (2005). Non-dissipative cloud transport in Eulerian grid models by the volume-of-fluid (VOF) method. *Atmospheric Environment* *39*, 4321–4330.
- Horn, S. (2012). ASAMgpu V1.0—a moist fully compressible atmospheric model using graphics processing units (GPUs). *Geosci. Model Dev.* *5*, 345–353.
- Ieda, T., Y. Kitamori, M. Mochida, R. Hirata, T. Hirano, K. Inukai, Y. Fujinuma, and K. Kawamura (2006). Diurnal variations and vertical gradients of biogenic volatile and semi-volatile organic compounds at the Tomakomai larch forest station in Japan. *Tellus* *59B*, 177–186.
- Kato, M. and B. E. Launder (1993). The modeling of turbulent flow around stationary and vibrating square cylinders. *Ninth Symposium on Turbulent Shear Flows*, 10.4.1–10.4.6. Kyoto, Japan.
- Kavouras, I. G., N. Mihalopoulos, and E. G. Stephanou (1999). Formation and gas/particle partitioning of monoterpenes photo-oxidation products over forests. *Geophysical Research Letters* *26*(1), 55–58.
-

Kulmala, M. (2003). How particles nucleate and grow. *Science* 302, 1000–1001.

Kulmala, M., A. Asmi, H. K. Lappalainen, U. Baltensperger, J.-L. Brenguier, M. C. Facchini, H.-C. Hansson, Ø. Hov, C. D. O’Dowd, U. Pöschl, A. Wiedensohler, R. Boers, O. Boucher, G. de Leeuw, H. A. C. Denier van der Gon, J. Feichter, R. Krejci, P. Laj, H. Lihavainen, U. Lohmann, G. McFiggans, T. Mentel, C. Pilinis, I. Riipinen, M. Schulz, A. Stohl, E. Swietlicki, E. Vignati, C. Alves, M. Amann, M. Ammann, A. S.;, P. Artaxo, H. Baars, D. C. S. Beddows, R. Bergström, J. P. Beukes, M. Bilde, J. F. Burkhardt, F. Canonaco, S. L. Clegg, H. Coe, S. Crumeyrolle, B. D’Anna, S. Decesari, S. Gilardoni, M. Fischer, A. M. Fjaeraa, C. Fountoukis, C. George, L. Gomes, P. Halloran, T. Hamburger, R. M. Harrison, H. Herrmann, T. Hoffmann, C. Hoose, M. Hu, A. Hyvärinen, U. Hörrak, Y. Iinuma, T. Iversen, M. Josipovic, M. Kanakidou, A. Kiendler-Scharr, A. Kirkevåg, G. Kiss, Z. Klimont, P. Kolmonen, M. Komppula, J.-E. Kristjánsson, L. Laakso, A. Laaksonen, L. Labonnote, V. A. Lanz, K. E. J. Lehtinen, L. V. Rizzo, R. Makkonen, H. E. Manninen, G. McMeeking, J. Merikanto, A. Minikin, S. Mirme, W. T. Morgan, E. Nemitz, D. O’Donnell, T. S. Panwar, H. Pawlowska, A. Petzold, J. J. Pienaar, C. Pio, C. Plass-Duelmer, A. S. H. Prévôt, S. Pryor, C. L. Reddington, G. Roberts, D. Rosenfeld, J. Schwarz, Ø. Seland, K. Sellegri, X. J. Shen, M. Shiraiwa, H. Siebert, B. Sierau, D. Simpson, J. Y. Sun, D. Topping, P. Tunved, P. Vaattovaara, V. Vakkari, J. P. Veefkind, A. Visschedijk, H. Vuollekoski, R. Vuolo, B. Wehner, J. Wildt, S. Woodward, D. R. Worsnop, G.-J. van Zadelhoff, A. A. Zardini, K. Zhang, P. G. van Zyl, V.-M. Kerminen, K. S. Carslaw, and S. N. Pandi (2011). General overview: European Integrated project on Aerosol Cloud Climate and Air Quality interactions (EUCAARI) – integrating aerosol research from nano to global scales. *Atmos. Chem. Phys.* 11, 13061–13143.

Kulmala, M., K. Hämeri, P. P. Aalto, J. M. Mäkelä, L. Pirjola, D. E. Nilsson, G. Buzorius, Ü. Rannik, M. Dal Maso, W. Seidl, T. Hoffman, R. Janson, H.-C. Hansson, Y. Viisanen, A. Laaksonen, and C. D. O’Dowd (2001). Overview of the

- international project on biogenic aerosol formation in the boreal forest (BIOFOR). *Tellus 53B*, 324–343.
- Lohmann, U. and J. Feichter (2005). Global indirect aerosol effects: a review. *Atmos. Chem. Phys.* 5, 715–737.
- Louis, J.-F. (1979). A parametric model of vertical eddy fluxes in the atmosphere. *Boundary-Layer Meteorol.* 17, 187–202.
- Makkonen, R., A. Asmi, V.-M. Kerminen, M. Boy, A. Arneth, A. Guenther, and M. Kulmala (2012). BVOC-aerosol-climate interactions in the global aerosol-climate model ECHAM5.5-HAM2. *Atmos. Chem. Phys.* 12, 10077–10096.
- Makkonen, R., A. Asmi, V.-M. Kerminen, M. Boy, A. Arneth, P. Hari, and M. Kulmala (2012). Air pollution control and decreasing new particle formation lead to strong climate warming. *Atmos. Chem. Phys.* 12, 1515–1524.
- Massman, W. J. and J. C. Weil (1999). An analytical one-dimensional second-order closure model of turbulence statistics and the lagrangian time scale within and above plant canopies of arbitrary structure. *Boundary-Layer Meteorol.* 91, 81–107.
- Moeng, C.-H. (1984). A Large-Eddy-Simulation model for the study of planetary boundary-layer turbulence. *J. Atmos. Sci.* 41, 2052–2062.
- Moeng, C.-H., J. C. McWilliams, R. Rotunno, P. P. Sullivan, and J. C. Weil (2004). Investigating 2D modeling of atmospheric convection in the PBL. *J. Atmos. Sci.* 61, 889–903.
- Pachauri, R. and A. Reisinger (2007). Climate change 2007: Synthesis report. Technical Report 104, IPCC, Geneva, Switzerland.
- Ramanathan, V., P. J. Crutzen, J. T. Kiehl, and D. Rosenfeld (2001). Aerosols, Climate, and the Hydrological Cycle. *Science* 294, 2119–2124.
- Rannik, Ü., T. Markkanen, J. Raittila, P. Hari, and T. Vesala (2003). Turbulence statistics inside and over forest: influence on footprint prediction. *Boundary-Layer Meteorol.* 109, 163–189.
-

- Riipinen, I., J. R. Pierce, T. Yli-Juuti, T. Nieminen, S. A. K. Häkkinen, M. Ehn, H. Junninen, K. Lehtipalo, T. Petäjä, J. Slowik, R. Chang, N. C. Shantz, J. Abbatt, W. R. Leitch, V.-M. Kerminen, D. R. Worsnop, S. N. Pandis, N. M. Donahue, and M. Kulmala (2011). Organic condensation: a vital link connecting aerosol formation to cloud condensation nuclei (CCN) concentrations. *Atmos. Chem. Phys.* *11*, 3865–3878.
- Riipinen, I., T. Yli-Juuti, J. R. Pierce, T. Petäjä, D. R. Worsnop, M. Kulmala, and N. M. Donahue (2012). The contribution of organics to atmospheric nanoparticle growth. *Nature Geoscience* *5*, 453–458.
- Saiki, E. M., C.-H. Moeng, and P. P. Sullivan (2000). Large-Eddy Simulation of the stably stratified planetary boundary layer. *Boundary-Layer Meteorol.* *95*, 1–30.
- Schlegel, F., J. Stiller, A. Bienert, H.-G. Maas, R. Queck, and C. Bernhofer (2012). Large-Eddy Simulation of inhomogeneous canopy flows using high resolution terrestrial laser scanning data. *Boundary-Layer Meteorol.* *142*, 223–243.
- Seinfeld, J. H. and S. N. Pandis (2006). *Atmospheric Chemistry and Physics: From Air Pollution to Climate Change*. John Wiley and Sons.
- Shaw, R. H. and U. Shumann (1992). Large-eddy simulation of turbulent flow above and within a forest. *Boundary-Layer Meteorol.* *61*, 47–64.
- Shen, S. and M. Leclerc (1997). Modelling the turbulence structure in the canopy layer. *Agric. For. Meteorol.* *87(1)*, 3–25.
- Sogachev, A. (2009). A note on two-equation closure modelling of canopy flow. *Boundary-Layer Meteorol.* *130*, 423–435.
- Sogachev, A., G. Menzhulin, M. Heimann, and J. Lloyd (2002). A simple three dimensional canopy – planetary boundary layer simulation model for scalar concentrations and fluxes. *Tellus* *54B*, 784–819.

Tarvainen, V., H. Hakola, H. Hellén, J. Bäck, P. Hari, and M. Kulmala (2005). Temperature and light dependence of the VOC emissions of Scots pine. *Atmos. Chem. Phys.* 5, 989–998.

Yue, W., M. B. Parlange, C. Meneveau, W. Zhu, R. Hout, and J. Katz (2007). Large-eddy simulation of plant canopy flows using plant-scale representation. *Boundary-Layer Meteorol.* 124(2), 183–203.

